

DIRECT VS. SYNAPTIC COUPLING IN A MATHEMATICAL MODEL OF CYTONEME-BASED MORPHOGEN GRADIENT FORMATION*

HYUNJOONG KIM[†] AND PAUL C. BRESSLOFF[†]

Abstract. In developmental biology, an important problem is understanding the mechanisms underlying the formation of morphogen concentration gradients. The most commonly hypothesized mechanism involves the diffusion and degradation of morphogens from a localized source. Recently, however, an alternative mechanism has been proposed, which is based on cell-to-cell contacts mediated by thin, actin-rich cellular extensions known as cytonemes. In this paper, we develop a one-dimensional advection-diffusion transport model of cytoneme-based morphogenesis. In particular, we compare two distinct types of contact between a cytoneme tip and a target cell: direct contact and indirect contact mediated by a synapse. First, we calculate the steady-state concentration profiles and show that synaptic contacts generate broader concentration profiles, thus allowing for longer-range interactions. We then consider two alternative methods for determining how quickly the system approaches steady-state: either calculating the accumulation time using Laplace transforms, or analyzing the discrete spectrum of the associated evolution operator. The latter is a nontrivial eigenvalue problem due to the nature of the boundary conditions. Finally, we extend the direct contact model to the case of a stochastically switching boundary at the cytoneme tip, in order to take into account the fact that cytonemes dynamically grow and shrink, resulting in more temporary contacts with target cells.

Key words. advection-diffusion, morphogenesis, cytoneme, boundary value problem

AMS subject classifications. 92C15, 92C3, 35K20

DOI. 10.1137/18M1179699

1. Introduction. An important problem in developmental biology is understanding the mechanisms underlying the formation and maintenance of morphogen concentration gradients [29]. Such gradients drive the discrete spatial patterning of differentiated gene expression across a cell population. The most commonly hypothesized mechanism of morphogen gradient formation involves the extracellular diffusion of morphogens away from a localized source of protein production. When this is combined with removal of proteins from the diffusing pool via degradation or binding to membrane-bound receptors, one obtains steady-state concentration profiles that decay exponentially (or algebraically) away from the source [15, 1, 27, 16, 22, 25]. Recently, however, an alternative mechanism for delivering morphogens to embryonic cells has been proposed, based on cell-to-cell contacts that are mediated by signaling filopodia known as *cytonemes* [12, 13, 14]. Cytonemes are thin, dynamic, actin-rich cellular extensions with a diameter of around 100 nm and lengths that vary from 1 to 100 μm .

Cytonemes were first characterized in the wing imaginal disc of *Drosophila* [18] and have been associated with the transport of both morphogenetic protein Decapentaplegic (Dpp) and Hedgehog (Hh) [19, 4, 12]. Many cytonemes in *Drosophila* are found to extend from morphogen-producing cells to target cells. Morphogens are

*Received by the editors April 10, 2018; accepted for publication (in revised form) July 5, 2018; published electronically September 4, 2018.

<http://www.siam.org/journals/siap/78-5/M117969.html>

Funding: The second author's work was supported by the National Science Foundation (DMS-1613048).

[†]Department of Mathematics, University of Utah, Salt Lake City, UT 84112 (hkim@math.utah.edu, bressloff@math.utah.edu).

actively transported along the cytonemes in a bidirectional fashion, probably via myosin motors that actively “walk” along the actin filaments of a cytoneme. The amount of morphogen delivered to a cell will then depend on the flux of particles along a cytoneme and the number of cytonemes that form a stable contact with the target cell. Cytonemes can also emanate from receptor-bearing target cells, transporting their receptors to the vicinity of source cells. Increasing experimental evidence indicates that cytonemes also mediate morphogen transport in vertebrates [11, 21]. Examples include sonic hedgehog (Shh) cell-to-cell signaling in chicken limb buds [20] and Wnt signaling in zebrafish [23, 24]. The latter involves a different morphogen transport mechanism, in which Wnt is clustered at the membrane tip of growing signaling filopodia. When the filopodia make contact with target cells, the morphogens are delivered to the cells and the filopodia are pruned off within 10 minutes of making contact. In this case, the amount of morphogen delivered to a cell will depend on the rate of filopodia growth, the concentration of morphogen at the tips, and the frequency of contacts between source and target cells. It is important to note, however, that very little is currently known about the precise biochemical and physical nature of the contacts between signaling filopodia such as cytonemes and their target cells [13, 10]. Important unresolved issues include how tips find their targets, how they are stabilized at their contact sites, and how morphogens are transferred to a receiving cell and subsequently internalized. For example, do cytonemes form a direct contact with a receiving cell or an indirect synaptic contact? Mathematical modeling can thus help in exploring the efficacy of various hypothesized mechanisms.

So far there has been very little modeling of cytoneme-based morphogenesis, particularly compared to diffusion-based morphogenesis. Recently, however, we introduced a model of the motor-based transport of morphogens along a collection of cytonemes of varying lengths, linking a source cell to a one-dimensional array of target cells [9]. Each cytoneme was assumed to form a fixed, direct physical contact with its corresponding target cell. This built upon a previous compartmental model of Teimouri and Kolomeisky [25, 26]. More specifically, we considered a simple bidirectional motor transport model, in which active particles carrying morphogens randomly switched between anterograde and retrograde transport. We took active particles to be injected at a rate that was proportional to the particle concentration in the source cell, and we imposed an absorbing boundary condition at the target end. Solving the steady-state solution of the transport equations, we calculated the length-dependent flux through each cytoneme and thus established how the system could support a morphogen concentration gradient that decays exponentially from the source. The existence of an explicit transport model also allowed us to determine the accumulation time of the morphogen gradient and its robustness to fluctuations in the rate of morphogen production in the source cell. One major observation of both modeling studies [25, 9] is that, although cytoneme-based gradient formation is potentially more precise than gradients that are diffusion-based, it comes at an energy cost.

In this paper, we further develop our mathematical modeling of cytoneme-based morphogenesis by investigating how the morphogen gradient depends on the nature of cell-to-cell contacts, specifically, direct vs. synaptic coupling. In the latter case, we assume that a cytoneme delivers vesicles of morphogen to a presynaptic vesicular pool. The vesicles are then released into the synaptic cleft via exocytosis and subsequently internalized by the target cell via endocytosis. This requires modifying the boundary condition at the cytoneme tip. For simplicity, we represent transport of morphogens along cytonemes in terms of advection-diffusion rather than bidirectional

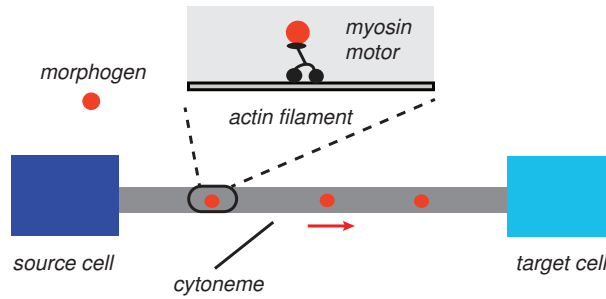


FIG. 2.1. Schematic diagram showing active motor-driven transport of morphogens along a cytoneme of fixed length.

transport. (The former can be obtained as an approximation of the full bidirectional model using a quasi-steady-state reduction [17]. It is important to note, however, that one would not recover the standard diffusion-based model of morphogenesis in the absence of advection, due to the nontrivial nature of the boundary conditions.) In section 2, we explore the consequences of the modified boundary condition on the steady-state morphogen gradient. In section 3, we use Laplace transforms to calculate the analog of the accumulation time considered in diffusion-based mechanisms [2, 3], which is important in order to check that the time to establish a morphogen gradient is consistent with developmental stages. In section 4, we consider an alternative characterization of the approach to steady-state, based on the spectrum of the associated evolution operator. This is a nontrivial boundary value problem due to the coupling between the cytoneme and the cellular compartments, which we analyze using winding numbers. Finally, in section 5 we further extend our direct coupling model by taking the transfer of vesicles from the cytoneme tip to the target cell to be stochastically gated. This is motivated by the observation that many cytonemes are not static objects, but dynamically grow and shrink, resulting in more temporary contacts with target cells. We analyze the stochastic model along analogous lines to recent studies of diffusion equations in domains with randomly switching boundaries [6, 7, 8], and show that dynamic contacts can lead to nonmonotonic concentration profiles.

2. Single cytoneme with direct or synaptic coupling. Consider a one-dimensional model of a single cytoneme of length L linking a source cell to a single target cell along the lines shown in Figure 2.1. Let $u(x, t)$ denote the density per unit length of motor-cargo particles at position $x \in [0, L]$ along the cytoneme and time t . Each particle is assumed to carry a vesicle containing morphogens. In our previous model, we partitioned the complexes into anterograde (+) and retrograde (−) subpopulations labeled by $u_+(x, t)$ and $u_-(x, t)$, respectively, and assumed that particles could switch between the two motile states according to a two-state Markov process. In order to incorporate more general boundary conditions, we will consider a simpler advection-diffusion model of active transport in this paper. The density $u(x, t)$ thus evolves according to the equation

$$(2.1) \quad \frac{\partial u}{\partial t} = -v \frac{\partial u}{\partial x} + D \frac{\partial^2 u}{\partial x^2}, \quad x \in (0, L),$$

where v is the average speed of motor-cargo transport and D is a diffusion coefficient. Equation (2.1) is supplemented by boundary conditions at the ends $x = 0, L$, which

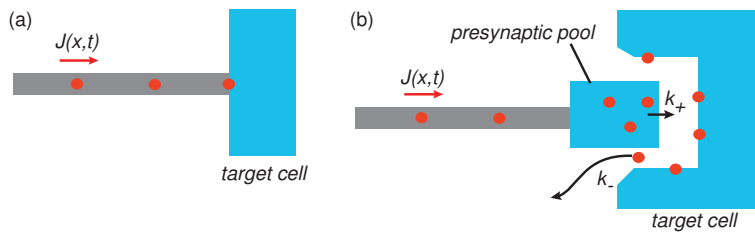


FIG. 2.2. Two forms of contact between a cytoneme tip and a target cell. (a) Direct coupling. (b) Indirect synaptic coupling.

will depend on the form of coupling between the cytoneme tip and the target cell. We consider two distinct cases.

2.1. Direct coupling model. This case was considered in [9]. In particular, we take

$$(2.2) \quad u(0, t) = \kappa C_0(t), \quad u(L, t) = 0,$$

where $C_0(t)$ is the density of vesicles in the source cell and κ is a constant with units of inverse length. The cytoneme tip is assumed to make direct physical contact with the target cell (see Figure 2.2(a)) such that all vesicles reaching the tip are immediately transferred to the target cell membrane for subsequent internalization; this is implemented by imposing an absorbing boundary condition at $x = L$. The interpretation of the boundary condition at $x = 0$ is less straightforward. Recall that we are modeling the active transport of vesicles rather than the passive diffusion of individual proteins. Thus, one should not interpret the boundary condition $u(0, t) = \kappa C_0(t)$ as a continuity equation for particles, in which $\kappa = A/V \ll 1$, where A is the cross-sectional area of the cytoneme and V is the volume of the source cell. Instead, we expect the vesicles to be targeted to some local region around the entrance of the cytoneme, where they are loaded onto molecular motors for transport. In our model we assume that the density of motor-cargo complexes at the entrance is proportional to the number of vesicles at the base of the cytoneme. The transport component of the model couples to the number of vesicles in the source and target cells, $C_{0,1}(t)$, according to

$$(2.3) \quad \frac{dC_0}{dt} = Q - J(0, t), \quad \frac{dC_1}{dt} = J(L, t) - kC_1(t),$$

where Q is the particle production rate in the source cell, k is a degradation rate, and $J(x, t)$ is particle flux at position x at time t :

$$(2.4) \quad J(x, t) = vu(x, t) - D \frac{\partial u(x, t)}{\partial x}.$$

(Note that morphogen concentrations can be obtained from vesicle concentrations by multiplying the latter by the mean number of proteins per vesicle.) Equations (2.3) are supplemented by the initial conditions $C_{0,1}(0) = 0$.

We now calculate the stationary solutions C_0^*, C_1^* as a function of cytoneme length. Setting the time derivative in (2.1) to zero yields $u = u(x)$ with

$$0 = -\frac{\partial}{\partial x} \left(vu - D \frac{\partial u}{\partial x} \right).$$

It follows that there is a constant stationary flux $J(x) = J^*$. Setting $dC_0/dt = 0$ in the first equation of (2.3) implies that $J^* = J(0) = Q$ so that

$$vu(x) - D \frac{\partial u(x)}{\partial x} = Q.$$

Imposing the left-hand boundary condition equation (2.2) then gives the solution

$$(2.5) \quad u(x) = \kappa C_0^* e^{-\gamma x} + \frac{Q}{v} (1 - e^{-\gamma x}), \quad \gamma = -\frac{v}{D}.$$

Finally, applying the absorbing boundary condition at $x = L$ yields the result

$$(2.6) \quad C_0^* = \frac{Q}{w(L)}, \quad C_1^* = \frac{Q}{k},$$

where

$$(2.7) \quad w(L) := \frac{\kappa v e^{-\gamma L}}{e^{-\gamma L} - 1}.$$

Note that $w(L) > 0$, since $e^{-\gamma L} - 1$ has the same sign as v . An important quantity, which generalizes to the multicell case, is the ratio of the target and source densities,

$$(2.8) \quad \frac{C_1^*}{C_0^*} = \frac{w(L)}{k}.$$

The length-dependence of this ratio is determined by the function $w(L)$, which we identify as an effective cytoneme ‘‘conductance,’’ in the sense that larger $w(L)$ means that the cytoneme is more effective at transferring vesicles to the target cell.

Example plots of $w(L)$ as a function of cytoneme length L are shown in Figure 2.3. As in our previous bidirectional model [9], we find that $w(L)$ is an exponentially decaying function of cytoneme length with the asymptotic value $\lim_{L \rightarrow \infty} w(L)$ depending on the sign of v . If $v < 0$ ($\gamma > 0$), then $w(L)$ decays to zero as cytoneme length tends to infinity, whereas if $v > 0$ ($\gamma < 0$), then $\lim_{L \rightarrow \infty} w(L) = \kappa v$. Irrespective of the sign of v , $w(L) \rightarrow \infty$ as $L \rightarrow 0$, which means that for arbitrarily short cytonemes, vesicles are immediately absorbed by the target cell so $C_0 = 0$. It is important to specify how the length-scale of the cytoneme relates to cell size. In the case of the *Drosophila* wing imaginal disc, cells are cylindrical in shape with a diameter of around 1 μm so that a cytoneme of length 10 μm can contact around 10 cells. One observation of the w -plots in Figure 2.3 is that the decay of $w(L)$ is quite sharp so that it has approximately reached its asymptotic value over the length spanned by just a few cells.

2.2. Synaptic coupling model. Now suppose that vesicles arriving at the presynaptic domain fill a presynaptic pool, which are then released into the synaptic cleft at a rate k_+ ; see Figure 2.2(b). Let $B_1(t)$ and $C_1(t)$ be the concentrations of vesicles in the presynaptic and postsynaptic domains, respectively. Then (2.3) becomes

$$(2.9) \quad \frac{dC_0}{dt} = Q - J(0, t), \quad \frac{dB_1}{dt} = J(L, t) - k_+ B_1(t), \quad \frac{dC_1}{dt} = -k_- C_1(t) + k_+ B_1(t),$$

where k_- is an effective degradation rate of postsynaptic vesicles, which could be due to failure to be endocytosed. In this case, (2.1) is supplemented by the boundary conditions

$$(2.10) \quad u(0, t) = \kappa C_0(t), \quad J(L, t) = \widehat{\kappa}[u(L, t) - \phi B_1(t)],$$

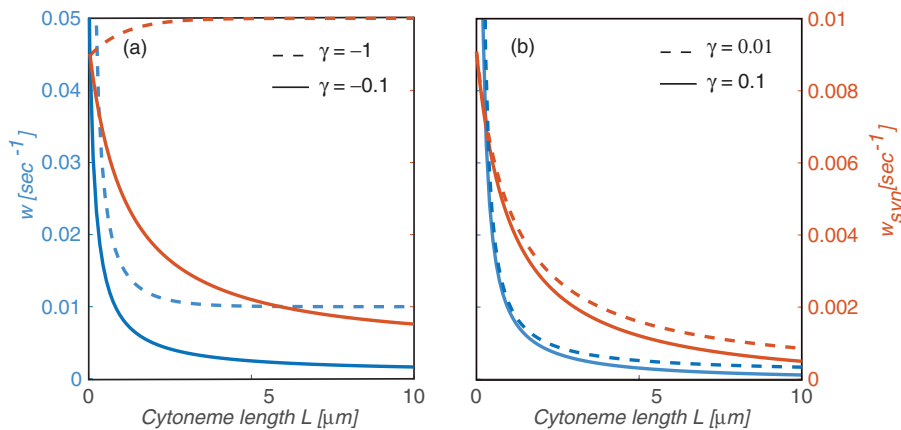


FIG. 2.3. “Conductance” of direct coupling model (blue or lighter curves) and synaptic coupling model (red or darker curves) for a single target cell. (a) Plots of $w(L)$ and $w_{\text{syn}}(L)$ against L for $\gamma < 0$. (b) Corresponding plots for $\gamma > 0$. Parameters are as follows: $D = 0.1\mu\text{m}^2\text{s}^{-1}$, $\kappa = 0.1\mu\text{m}^{-1}$, $\hat{\kappa} = 0.1\mu\text{m}\text{s}^{-1}$, $k = k_- = 0.8\text{s}^{-1}$, $k_+ = 1\text{s}^{-1}$, and $\phi = 1$. Transport speed $v = -\gamma D$.

where $\hat{\kappa}$ has units of velocity. That is, the flux into the presynaptic pool is proportional to the difference of concentrations at the pool entrance with ϕ some geometric factor. (Note that the direct coupling model can be recovered as follows. First, setting $k_{\pm} = k$ and taking the limit $k \rightarrow \infty$ implies that $C_1(t) = B_1(t)$; that is, we can identify the concentrations in the presynaptic and postsynaptic domains. Second, we take the limits $\hat{\kappa} \rightarrow \infty$ and $\phi \rightarrow 0$ so that we recover the absorbing boundary condition at the cytoneme tip.)

In the case of indirect synaptic coupling, we use the steady-state versions of (2.9) and (2.10) to determine C_0^* and C_1^* . In particular,

$$C_1^* = \frac{Q}{k_-}, \quad Q = \hat{\kappa} \left[u(L) - \frac{\phi k_-}{k_+} C_1^* \right],$$

which, on substituting into (2.5) for $x = L$, yields

$$(2.11) \quad \frac{\phi k_-}{k_+} C_1^* = \kappa C_0^* e^{-\gamma L} + \frac{Q}{v} [1 - e^{-\gamma L}] - \frac{Q}{\hat{\kappa}}.$$

This can be rearranged to show that

$$(2.12) \quad C_0^* = \frac{Q}{w_{\text{syn}}(L)}$$

with

$$(2.13) \quad w_{\text{syn}}(L) = \frac{\kappa v e^{-\gamma L}}{v/v_{\text{syn}} + e^{-\gamma L} - 1}, \quad v_{\text{syn}} = \left[\frac{\phi}{k_+} + \frac{1}{\hat{\kappa}} \right]^{-1}.$$

Here v_{syn} is the average speed of the synaptic process. We note that

$$\frac{dw_{\text{syn}}}{dL} = \gamma w_{\text{syn}}(L) \left[\frac{w_{\text{syn}}(L)}{\kappa v} - 1 \right].$$

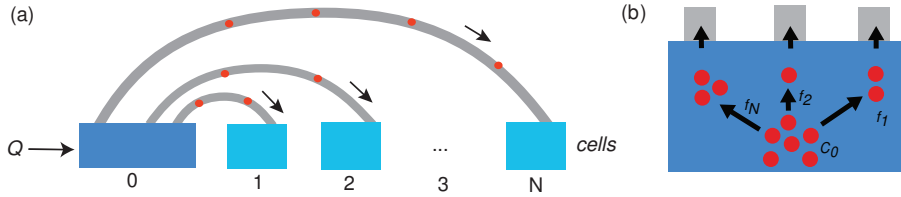


FIG. 2.4. (a) Schematic diagram of a one-dimensional array of target cells (labeled $n = 1, \dots, N$), each connected to a single source cell (labeled $n = 0$) via a cytoneme of length L_n . (b) Allocation of resources in the source cell with $f_n C_0$ particles localized to the n th cytoneme.

If $v < v_{\text{syn}}$, then $w_{\text{syn}}(L) > \kappa v$ and $dw_{\text{syn}}/dL < 0$ for all L (monotonically decreasing function w_{syn}). On the other hand, if $v > v_{\text{syn}}$, then $w_{\text{syn}}(L) < \kappa v$ and $dw_{\text{syn}}/dL > 0$ for all L (monotonically increasing function w_{syn}). In other words, if the transport speed is faster than the synaptic process speed, then the vesicles tend to accumulate in the synapse, slowing down the approach to steady-state. Also note that $w_{\text{syn}}(0) = \kappa v_{\text{syn}} < \infty$, which reflects the fact that the transfer of vesicles to the target cell is not instantaneous, even for arbitrarily short cytonemes. Example plots of $w_{\text{syn}}(L)$ are shown in Figure 2.3. It can be seen that for the same transport parameter values, the synaptic coupling supports a slower spatial decay of the conductance.

2.3. Multiple target cells. It is relatively straightforward to extend the single cytoneme model to multiple cytonemes of length L_n linking a source cell to multiple target cells, $n = 1, \dots, N$; see Figure 2.4(a). Let $u_n(x, t)$ be the density of transport particles in the cytoneme contacting the n th target cell. Then the advection-diffusion model for u_n on $x \in (0, L_n)$ takes the same form:

$$(2.14) \quad \frac{\partial u_n}{\partial t} = -v \frac{\partial u_n}{\partial x} + D \frac{\partial^2 u_n}{\partial x^2}.$$

In the case of direct coupling, the corresponding boundary conditions are

$$(2.15) \quad u_n(0, t) = \kappa f_n C_0(t), \quad u_n(L_n, t) = 0$$

with $\sum_n f_n = 1$. Here the coefficients f_n specify the allocation of resources to the n th cytoneme; see Figure 2.4(b). Extending (2.3) to the case of multiple target cells yields

$$(2.16) \quad \frac{dC_0}{dt} = Q - \sum_{m=1}^N J_m(0, t), \quad \frac{dC_n}{dt} = J_n(L_n, t) - kC_n,$$

where

$$J_n(x, t) = v u_n(x, t) - D \frac{\partial u_n(x, t)}{\partial x}.$$

Solving the stationary equations shows that $J_n(x) = J_n^*$, where J_n^* is the stationary flux reaching the n th target cell and

$$(2.17) \quad u_n(x) = \kappa f_n C_0^* e^{-\gamma x} + \frac{J_n^*}{v} [1 - e^{-\gamma x}].$$

Imposing the right-hand boundary conditions $u_n(L_n) = 0$ for $n = 1, \dots, N$ shows that $J_n^* = f_n C_0^* w(L_n)$ with $w(L)$ given by (2.7). Finally, the stationary versions of (2.16) implies

$$Q = \sum_{n=1}^N J_n^*, \quad C_n^* = \frac{J_n^*}{k},$$

that is,

$$(2.18) \quad C_0^* = \frac{Q}{\sum_{m=1}^N f_m w(L_m)}, \quad C_n^* = \frac{Q}{k} \frac{f_n w(L_n)}{\sum_{m=1}^N f_m w(L_m)}.$$

Equation (2.18) implies

$$(2.19) \quad \frac{C_n^*}{C_0^*} = \frac{f_n}{k} w(L_n),$$

where $w(L_n)$ is the conductance of a single cytoneme of length L_n .

An analogous result holds for indirect synaptic coupling. That is, (2.9) and (2.10) become

$$(2.20) \quad \frac{dC_0}{dt} = Q - \sum_{m=1}^N J_m(0, t), \quad \frac{dB_n}{dt} = J_n(L_n, t) - k_+ B_n(t), \quad \frac{dC_n}{dt} = -k_- C_n(t) + k_+ B_n(t)$$

and

$$(2.21) \quad u_n(0, t) = \kappa f_n C_0(t), \quad J_n(L_n, t) = \hat{\kappa} [u_n(L_n, t) - \phi B_n(t)].$$

These yield the steady-state equations

$$C_n^* = \frac{J_n^*}{k_-}, \quad Q = \sum_{n=1}^N J_n^*, \quad J_n^* = \hat{\kappa} \left[u_n(L_n) - \frac{\phi k_-}{k_+} C_n^* \right],$$

which, on substituting into (2.17) for $x = L$, yield

$$(2.22) \quad \frac{\phi k_-}{k_+} C_n^* = \kappa f_n C_0^* e^{-\gamma L_n} + \frac{J_n^*}{v} [1 - e^{-\gamma L_n}] - \frac{J_n^*}{\hat{\kappa}}.$$

This can be rearranged to show that $J_n^* = f_n C_0^* w_{\text{syn}}(L_n)$ and thus

$$(2.23) \quad C_0^* = \frac{Q}{\sum_{m=1}^N f_m w_{\text{syn}}(L_m)}, \quad C_n^* = \frac{Q}{k_-} \frac{f_n w_{\text{syn}}(L_n)}{\sum_{m=1}^N f_m w_{\text{syn}}(L_m)}.$$

3. Accumulation time. One way to characterize the time-dependent approach to steady-state is to determine the accumulation time [2, 3]. Following our previous model [9], we introduce the function

$$G_1(t) = 1 - \frac{C_1(t)}{C_1^*},$$

which represents the fractional deviation of the concentration from the steady-state C_1^* . Assuming that $C_1(t)$ is smooth enough and $C_1(0) = 0$, then $1 - G_1(t)$ is the fraction of the steady-state concentration that has accumulated by time t . The accumulation time is then defined by analogy with mean first passage times:

$$(3.1) \quad \tau_1 = \int_0^\infty t \frac{d}{dt} (1 - G_1(t)) dt = \int_0^\infty G_1(t) dt.$$

The accumulation time can be calculated using Laplace transforms. That is, defining

$$\hat{G}_1(s) = \int_0^\infty G_1(t)e^{-st} dt,$$

we have $\tau_1 = \lim_{s \rightarrow 0} \hat{G}(s)$. Integration by parts yields that $\lim_{s \rightarrow 0} s\hat{C}_1(s) = C_1^*$. Then we have

$$(3.2) \quad \tau_1 = \lim_{s \rightarrow 0} \frac{1}{s} \left(1 - \frac{s\hat{C}_1(s)}{C_1^*} \right) = -\frac{1}{C_1^*} \frac{d}{ds} s\hat{C}_1(s) \Big|_{s=0}.$$

3.1. Direct coupling model. Taking Laplace transforms of the second equation in (2.3) gives

$$s\hat{C}_1(s) = \frac{s}{s+k} \hat{J}(L, s).$$

Substituting this into (3.2) and using

$$\lim_{s \rightarrow 0} s\hat{J}(L, s) = \lim_{t \rightarrow \infty} J(L, t) = Q = kC_1^*,$$

we obtain

$$(3.3) \quad \tau_1 = \frac{1}{k} - \frac{1}{Q} \frac{d}{ds} s\hat{J}(L, s) \Big|_{s=0}.$$

Now we want to find $\hat{u}(x, s)$. Taking Laplace transform of (2.1) yields

$$\partial_x^2 \hat{u}(x, s) + \gamma \partial_x \hat{u}(x, s) = \frac{s}{D} \hat{u}(x, s),$$

and the corresponding general solution is given by

$$(3.4) \quad \hat{u}(x, s) = e^{-\frac{1}{2}\gamma x} [A(s) \sinh(\gamma_1(s)x) + B(s) \cosh(\gamma_1(s)x)],$$

where

$$(3.5) \quad \gamma_1(s) = \sqrt{\left(\frac{\gamma}{2}\right)^2 + \frac{s}{D}}$$

and the coefficients $A(s), B(s)$ are determined by the boundary conditions (2.2).

Taking the time derivative of the boundary condition at $x = 0$ and Laplace transforming, we have

$$(3.6) \quad s\hat{u}(0, s) = \kappa \left[\frac{Q}{s} - \hat{J}(0, s) \right].$$

The Laplace transform of $J(x, t)$ is

$$\hat{J}(x, s) = -D [\partial_x \hat{u}(x, s) + \gamma \hat{u}(x, s)],$$

and using the general solution (3.4), this gives

$$(3.7) \quad \hat{J}(x, s) = -D \left[\frac{\gamma}{2} \hat{u}(x, s) + e^{-\frac{1}{2}\gamma x} \gamma_1 (A(s) \cosh(\gamma_1 x) + B(s) \sinh(\gamma_1 x)) \right].$$

Substituting (3.4) and (3.7) at $x = 0$ into (3.6) yields

$$(3.8) \quad sB(s) = \kappa \left[\frac{Q}{s} + D \left(\frac{\gamma B(s)}{2} + \gamma_1(s)A(s) \right) \right].$$

Similarly, Laplace transforming the remaining boundary condition at $x = L$ gives

$$(3.9) \quad A(s) \sinh[\gamma_1(s)L] + B(s) \cosh[\gamma_1(s)L] = 0.$$

Solving (3.8) and (3.9) for $A(s)$ and $B(s)$, we have

$$(3.10) \quad A(s) = -\frac{\kappa Q \cosh[\gamma_1(s)L]}{s\mathcal{A}(L, s)}, \quad B(s) = \frac{\kappa Q \sinh[\gamma_1(s)L]}{s\mathcal{A}(L, s)},$$

where

$$\mathcal{A}(L, s) = \kappa D \gamma_1(s) \cosh[\gamma_1(s)L] + \left(s + \frac{\kappa v}{2} \right) \sinh[\gamma_1(s)L].$$

Substituting (3.10) into (3.7) at $x = L$ and imposing a hyperbolic-trigonometric identity gives

$$\frac{s\hat{J}(L, s)}{Q} = \kappa D e^{-\frac{1}{2}\gamma L} \cdot \frac{\gamma_1(s)}{\mathcal{A}(L, s)}.$$

Finally, substituting into (3.3) and evaluating the derivative with respect to s gives

$$(3.11) \quad \tau_1 = \frac{1}{k} + \frac{D}{\kappa v^2} [\kappa(e^{\gamma L} - 1 - \gamma L) + \gamma(e^{\gamma L} - 1)].$$

The asymptotic behavior of the accumulation time depends on sign of v ; see Figure 3.1(a). If $v > 0$ so that $\gamma < 0$, then

$$\lim_{L \rightarrow \infty} \frac{\tau_1(L)}{L} = \frac{1}{v},$$

that is, $\tau_1(L)$ increases linearly with respect to L . This reflects the fact that for positive speeds v , the dynamics behaves like a particle moving with constant velocity. On the other hand, if $v < 0$ so that $\gamma > 0$, then diffusion dominates and $\tau_1(L)$ increases exponentially.

3.2. Synaptic coupling model. In a similar fashion, we can evaluate the accumulation time $\tau_{1,\text{syn}}$ of the synaptic coupling model. First, Laplace transforming the last equation in (2.9), we have

$$s\hat{C}_1(s) = \frac{k_+}{s + k_-} s\hat{B}_1(s).$$

Substituting this into (3.2) and using $k_+B_1^* = k_-C_1^*$ gives

$$(3.12) \quad \tau_{1,\text{syn}} = \frac{1}{k_-} - \frac{1}{B_1^*} \frac{d}{ds} s\hat{B}_1(s) \Big|_{s=0}.$$

It remains to find $\hat{B}_1(s)$. Taking Laplace transforms of the second equation in (2.9) and using the right-hand boundary condition (2.10) yields

$$(3.13) \quad s\hat{B}_1(s) = \frac{\hat{\kappa}}{s + \hat{\kappa}\phi + k_+} s\hat{u}(L, s).$$

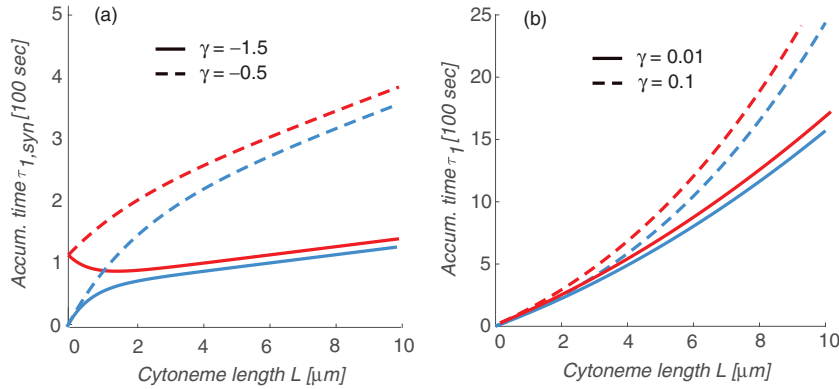


FIG. 3.1. Accumulation time of direct coupling model (blue or lighter curves) and synaptic coupling model (red or darker curves) for a single target cell and various values of γ . (a) Plots of the accumulation times τ_1 and $\tau_{1,syn}$ for $\gamma < 0$. (b) Corresponding plots for $\gamma > 0$. Other parameter values as Figure 2.3.

Applying the steady-state solution $\hat{\kappa}u(L) = (\hat{\kappa}\phi + k_+)B_1^*$ shows that

$$(3.14) \quad -\frac{1}{B_1^*} \frac{d}{ds} s\hat{B}_1(s) \Big|_{s=0} = \frac{1}{\hat{\kappa} + k_+} - \frac{1}{u(L)} \frac{d}{ds} s\hat{u}(L, s) \Big|_{s=0}.$$

Substituting (3.14) into (3.12), we have

$$(3.15) \quad \tau_{1,syn} = \frac{1}{k_-} + \frac{1}{\hat{\kappa}\phi + k_+} - \frac{1}{u(L)} \frac{d}{ds} s\hat{u}(L, s) \Big|_{s=0}.$$

We now want to calculate $\hat{u}(L, s)$. Since the synaptic coupling model shares the transport equation (2.1) with the direct coupling model, we can utilize the same general solutions (3.4) and (3.7) for $\hat{u}(x, s)$ and $\hat{J}(x, s)$, respectively, but with new coefficients $A_{syn}(s)$ and $B_{syn}(s)$, which are determined by the boundary conditions (2.10). Furthermore, since the two models have the same boundary condition at $x = 0$ and the same dynamics for $C_0(t)$, it follows that $A_{syn}(s)$ and $B_{syn}(s)$ are related according to (3.8). Turning to the boundary condition at $x = L$, we Laplace transform the second equation in (2.10) and use (3.13) to give

$$(3.16) \quad \hat{J}(L, s) = \frac{\hat{\kappa}(s + k_+)}{s + \hat{\kappa}\phi + k_+} \hat{u}(L, s).$$

Using (3.4) and (3.7) at $x = L$, we find that

$$(3.17) \quad \begin{aligned} & [\gamma_2(s) \sinh(\gamma_1(s)L) - \gamma_1(s) \cosh(\gamma_1(s)L)] A_{syn}(s) \\ &= [\gamma_1(s) \sinh(\gamma_1(s)L) - \gamma_2(s) \cosh(\gamma_1(s)L)] B_{syn}(s), \end{aligned}$$

where $\gamma_1(s)$ is given by (3.5) and

$$D\gamma_2(s) = \frac{v}{2} - \frac{\hat{\kappa}(s + k_+)}{s + \hat{\kappa}\phi + k_+}.$$

Now solving (3.8) and (3.17) for $A_{\text{syn}}(s)$ and $B_{\text{syn}}(s)$ leads to

$$(3.18a) \quad A_{\text{syn}}(s) = \frac{\kappa Q}{s \mathcal{A}_{\text{syn}}} [\gamma_1 \sinh(\gamma_1 L) - \gamma_2 \cosh(\gamma_1 L)],$$

$$(3.18b) \quad B_{\text{syn}}(s) = \frac{\kappa Q}{s \mathcal{A}_{\text{syn}}} [\gamma_2 \sinh(\gamma_1 L) - \gamma_1 \cosh(\gamma_1 L)],$$

where

$$\begin{aligned} \mathcal{A}_{\text{syn}}(L, s) &= \kappa D \gamma_1(s) \cdot [\gamma_2(s) \cosh(\gamma_1(s)L) - \gamma_1(s) \sinh(\gamma_1(s)L)] \\ &\quad + \left(s + \frac{\kappa v}{2} \right) \cdot [\gamma_2(s) \sinh(\gamma_1(s)L) - \gamma_1(s) \cosh(\gamma_1(s)L)]. \end{aligned}$$

Substituting (3.18) into the general solution (3.4) at $x = L$ and imposing hypertrigonometric identities gives

$$(3.19) \quad \frac{s \hat{u}(L, s)}{u(L)} = -\kappa e^{-\frac{1}{2}\gamma L} \frac{\gamma_1(s)}{\mathcal{A}_{\text{syn}}(L, s)} \cdot \frac{Q}{u(L)}.$$

Multiplying (3.16) by s and taking $s \rightarrow 0$ proves that

$$(3.20) \quad Q = \lim_{t \rightarrow \infty} J(L, t) = \lim_{s \rightarrow 0} s \hat{J}(L, s) = \frac{u(L)}{1/\hat{\kappa} + \phi/k_+}.$$

Therefore, combining (3.19), (3.20), and (3.15) yields

$$(3.21) \quad \tau_{1,\text{syn}} = \frac{1}{k_-} + \frac{1}{\hat{\kappa}\phi + k_+} + \frac{\kappa e^{-\frac{1}{2}\gamma L}}{1/\hat{\kappa} + \phi/k_+} \frac{d}{ds} \frac{\gamma_1(s)}{\mathcal{A}_{\text{syn}}(L, s)} \Big|_{s=0}.$$

Example plots of $w_{\text{syn}}(L)$ are shown in Figure 3.1. It can be seen that the asymptotic behavior of the accumulation time is similar to the direct coupling model. If $v > 0$, then $\tau_{1,\text{syn}}$ is asymptotically linear with respect to L . On the other hand, if $v < 0$, then $\tau_{1,\text{syn}}$ is exponentially increasing with respect to L . In the former case, $\tau_{1,\text{syn}}$ can be a nonmonotonic function of L . In general $w_{\text{syn}}(L) > w(L)$ due to the extra processing time at a synapse.

4. Spectral analysis. The existence of a finite accumulation time suggests that the steady-state is stable. Another way to establish stability and characterize the approach to steady-state is to determine the spectrum of the linear evolution operator. One then expects the principal nonzero eigenvalue to dominate the asymptotic approach to steady-state. In this section, we analyze the eigenvalues of the linearized equations for both the direct coupling and synaptic coupling models and relate the leading order asymptotic behavior with the accumulation time.

4.1. Direct coupling model. Consider perturbations about the steady-state $(u(x), C_0^*, C_1^*)$,

$$u(x, t) = u(x) + e^{\lambda t} \omega(x), \quad C_i(t) = C_i^* + e^{\lambda t} \psi_i, \quad i = 0, 1.$$

Substituting into the direct coupling model gives

$$(4.1a) \quad \partial_x^2 \omega(x) + \gamma \partial_x \omega(x) = \frac{\lambda}{D} \omega(x), \quad 0 < x < L,$$

$$(4.1b) \quad \partial_x \omega(0) + \gamma \omega(0) = \frac{\lambda}{D} \psi_0,$$

$$(4.1c) \quad \partial_x \omega(L) + \gamma \omega(L) = -\frac{\lambda + k}{D} \psi_1$$

and

$$(4.2) \quad \omega(0) = \kappa\psi_0, \quad \omega(L) = 0.$$

The corresponding general solution of (4.1a) is

$$(4.3) \quad \omega(x) = e^{-\frac{1}{2}\gamma x} [A \sinh(\gamma_1(\lambda)x) + B \cosh(\gamma_1(\lambda)x)],$$

where the function γ_1 is given by (3.5) and A, B are coefficients. Imposing the boundary conditions (4.2) determines A and B such that

$$(4.4) \quad \omega(x) = \kappa\psi_0 e^{-\frac{1}{2}\gamma x} \cdot \frac{\sinh[\gamma_1(\lambda)(L-x)]}{\sinh(\gamma_1(\lambda)L)}.$$

Substituting (4.4) into (4.1b) and (4.1c) leads to the pair of equations

$$(4.5) \quad \frac{\gamma}{2} - \gamma_1(\lambda) \coth[\gamma_1(\lambda)L] = \frac{\lambda}{\kappa D}$$

and

$$(4.6) \quad \kappa e^{-\frac{1}{2}\gamma L} \frac{\gamma_1(\lambda)}{\sinh[\gamma_1(\lambda)L]} \psi_0 = \frac{\lambda + k}{D} \psi_1.$$

Equation (4.5) is a transcendental equation for the eigenvalues λ , whereas (4.6) determines the eigenvector (ψ_0, ψ_1) corresponding to λ (up to scalar multiplication). Note that the linear operator of the boundary value problem given by (4.1a)–(4.1c) is not self-adjoint with respect to the L^2 inner product. Therefore, one cannot assume a priori that the eigenvalues are real.

In order to simplify the analysis of (4.5), we set $z = \gamma_1(\lambda)^2 = \lambda/D + (\gamma/2)^2$ so that (4.5) can be rewritten as

$$(4.7) \quad f(z) := \kappa\sqrt{z} \coth(L\sqrt{z}) + z - \mathcal{G} = 0,$$

where $\mathcal{G}(\gamma) = (\gamma^2 + 2\kappa\gamma)/4$. The stability condition $Re(\lambda) < 0$ for all λ is equivalent to the condition $Re(z_0) < (\gamma/2)^2$, where z_0 is a root of $f(z)$. First, consider real roots. Since $f_0(z) := \kappa\sqrt{z} \coth(L\sqrt{z})$ is a real-valued function on $z \in \mathbb{R}$, real solutions of (4.7) are obtained by the intersection points of the two graphs $y = f_0(z)$ and $y = -z + \mathcal{G}$; see Figure 4.1. If there existed a root $z_0 > (\gamma/2)^2$, then $-\gamma^2/4 + \mathcal{G}(\gamma) > f_0\left(\frac{\gamma^2}{4}\right)$, that is,

$$\gamma \sinh\left(\frac{L|\gamma|}{2}\right) > |\gamma| \cosh\left(\frac{L|\gamma|}{2}\right) > 0.$$

Since there is no γ satisfying the inequality, it follows that all real roots satisfy the stability condition $Re(z_0) < (\gamma/2)^2$.

It remains to explore the roots in the complex plane that are not on the real axis, $\{z, Im(z) \neq 0\}$. We will use a winding number argument, which counts the number N_0 of roots in a region inside of a contour Γ . First, to find N_0 on the upper-half complex plane, we construct the counterclockwise contour Γ^+ consisting of the semi-circle $\Gamma_R^+ = \{z = Re^{-i\theta}, \delta < \theta < \pi - \delta\}$ and the rays $\Gamma_\delta = \{z = re^{i\delta}, 0 < r < R\}$, $\Gamma_{\pi-\delta} = \{z = (R-r)e^{i(\pi-\delta)}, 0 < r < R\}$; see Figure 4.2(a). Applying the argument principle to the function $f(z)$ on the contour Γ^+ gives

$$(4.8) \quad N_0 - N_\infty = W(f, \Gamma^+),$$

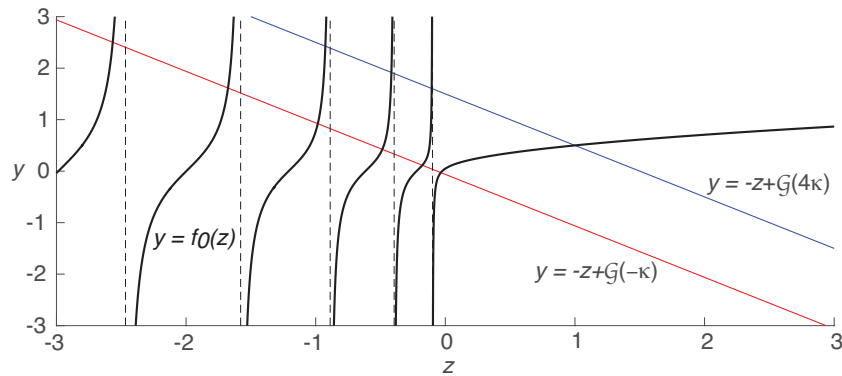


FIG. 4.1. Intersection of $y = f_0(z)$ and $y = -z + \mathcal{G}(\gamma)$ on $z \in \mathbb{R}$ for direct coupling model. The black solid line depicts the graph of $y = f_r(z)$, and the black dotted line shows its asymptotic lines. The blue line depicts the graph of $y = -z + \mathcal{G}(4\kappa)$, and the red line shows $y = -z + \mathcal{G}(-\kappa)$. Intersections of the black line and colored line gives solution of $f(z) = 0$ on the real line. Both colored lines have countably many solutions satisfying $z < (\gamma/2)^2$.

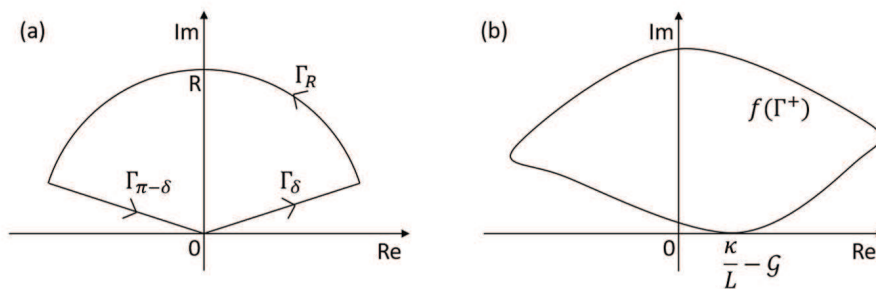


FIG. 4.2. Counterclockwise contour Γ^+ and its image $f(\Gamma^+)$. (a) Counterclockwise contour Γ^+ consisting of the semicircle $\Gamma_R^+ = \{z = Re^{-\theta}, \delta < \theta < \pi - \delta\}$ and the rays $\Gamma_\delta = \{z = re^{i\delta}, 0 < r < R\}$, $\Gamma_{\pi-\delta} = \{z = (R-r)e^{i(\pi-\delta)}, 0 < r < R\}$. (b) Image of the contour $f(\Gamma^+)$. This lies on the upper-half plane, and thus it cannot wind around the origin.

where $N_0(N_\infty)$ is the number of zeros (poles) of f inside Γ^+ and $W(f, \Gamma_+)$ is the winding number of $f(\Gamma_+)$ around the origin counterclockwise. In the following, we calculate N_∞ and $W(f, \Gamma_+)$ and thus determine N_0 . For the semicircle path Γ_R , as $R = |z| \rightarrow \infty$, we have

$$f(z) \approx z \left(1 + \kappa \frac{1}{\sqrt{z}} \cdot 1 - \frac{\mathcal{G}}{z} \right) \approx z,$$

and this implies that $f(\Gamma_R)$ is on the upper-half plane. For the ray Γ_δ , one can calculate the imaginary part of the parameterized curve $f(\Gamma_\delta)$:

$$\text{Im}[f \circ z(r)] = r \sin \delta + \frac{\kappa \sqrt{r}}{|\sinh(z(t))|^2} f_b(2L\sqrt{r}, \delta/2),$$

where

$$f_b(x, y) = \frac{1}{2} [\sin y \cdot \sinh(x \cos y) - \cos y \cdot \sin(x \sin y)].$$

Since $f_b(0, y) = 0$ and

$$\frac{df_b}{dx}(x, y) = \frac{\sin(2y)}{4} [\cosh(x \cos y) - \cos(x \sin y)] \geq \frac{\sin(2y)}{4} [\cosh(x \cos y) - 1] \geq 0$$

for $y > 0$, it follows that $f_b(x, y) \geq 0$ if $x, y > 0$ and, hence, $Im[f \circ z(r)] \geq 0$. This implies that $f(\Gamma_\delta)$ is on the upper-half plane. By substituting $r = R - r$ and $\delta = \pi - \delta$, one can also prove that $f(\Gamma_{\pi-\delta})$ is on the upper-half plane. Given that $f(\Gamma^+)$ is on the upper-half plane, $f(\Gamma_+)$ cannot wind around the the origin (see Figure 4.2(b)), and we have shown that $W(f, \Gamma^+) = 0$.

Finally, note that $f(z)$ has a removable singularity at the origin, since $\coth(\sqrt{z}L)$ varies as $1/\sqrt{z}$ as $z \rightarrow 0$. This implies that $N_\infty = 0$ for $0 < \delta \ll 1$ and $R > 0$, and thus $N_0 = N_\infty + W(f, \Gamma^+) = 0$ on the upper-half plane. Similarly, one can prove that $N_0 = 0$ on the lower-half plane. Therefore, there are no roots of f in $\{z, Im(z) \neq 0\}$, and the steady-state of the direct coupling model is unconditionally linearly stable.

4.2. Synaptic coupling model. Following along similar lines to the direct coupling model, consider perturbations of the steady-state solution $(u(x), C_0^*, B_1^*, C_1^*)$ of the synaptic coupling model:

$$u(x, t) = u(x) + e^{\lambda t} \omega(x), \quad C_i(t) = C_i^* + e^{\lambda t} \psi_i, \quad B_1(t) = B_1^* + e^{\lambda t} \sigma_1.$$

Substituting into the synaptic coupling model yields (4.1a) and (4.1b) together with

$$(4.9a) \quad \partial_x \omega(L) + \gamma \omega(L) = -\frac{\lambda + k_+}{D} \sigma_1,$$

$$(4.9b) \quad k_+ \sigma_1 = (\lambda + k_-) \psi_1,$$

and the boundary conditions

$$(4.10) \quad \omega(0) = \kappa \psi_0, \quad \partial_x \omega(L) + \gamma \omega(L) = \frac{\hat{\kappa}}{D} [\phi \sigma_1 - \omega(L)].$$

Again the general solution of (4.1a) is given by (4.3) with the coefficients A, B determined by the boundary conditions. We find that A and B satisfy the pair of equations

$$(4.11) \quad \gamma_1(\lambda)A + \left(\frac{\gamma}{2} - \frac{\lambda}{\kappa D}\right)B = 0$$

and

$$(4.12) \quad \mathcal{M}_1(\lambda)A + \mathcal{M}_2(\lambda)B = 0,$$

where

$$\begin{aligned} \mathcal{M}_1(\lambda) &= \gamma_3(\lambda) \sinh(\gamma_1(\lambda)L) + \gamma_1(\lambda) \cosh(\gamma_1(\lambda)L), \\ \mathcal{M}_2(\lambda) &= \gamma_3(\lambda) \cosh(\gamma_1(\lambda)L) + \gamma_1(\lambda) \sinh(\gamma_1(\lambda)L), \end{aligned}$$

and

$$\gamma_3(\lambda) = \frac{\hat{\kappa}}{D} \cdot \frac{\lambda + k_+}{\lambda + \hat{\kappa}\phi + k_+} + \frac{\gamma}{2}.$$

To obtain a nontrivial solution of the linear system (4.11) and (4.12), we require its determinant to be zero:

$$(4.13) \quad \gamma_1(\lambda)\mathcal{M}_2(\lambda) + \left(\frac{\lambda}{\kappa D} - \frac{\gamma}{2}\right)\mathcal{M}_1(\lambda) = 0.$$

In the same fashion as we did for direct coupling model, we investigate the linear stability of the steady-state solution by studying roots of (4.13) on the real line and showing that there is no root on the complex plane except the real axis. First, substituting $z = \lambda/D + (\gamma/2)^2$ into (4.13) yields

$$(4.14) \quad \sqrt{z}\widetilde{\mathcal{M}}_2(z) + \frac{1}{\kappa}(z - \mathcal{G})\widetilde{\mathcal{M}}_1(z) = 0,$$

where

$$\widetilde{\mathcal{M}}_1 = \tilde{\gamma}_3(z) \sinh(\sqrt{z}L) + \sqrt{z} \cosh(\sqrt{z}L), \quad \widetilde{\mathcal{M}}_2 = \tilde{\gamma}_3(z) \cosh(\sqrt{z}L) + \sqrt{z} \sinh(\sqrt{z}L),$$

and $\tilde{\gamma}_3(z) = \gamma_3(D(z - (\gamma/2)^2))$. Suppose that $\widetilde{\mathcal{M}}_1 \neq 0$. Then solving (4.14) is equivalent to finding a solution of

$$(4.15) \quad 0 = \frac{\kappa\sqrt{z}\widetilde{\mathcal{M}}_2(z)}{\widetilde{\mathcal{M}}_1(z)} + z - \mathcal{G} := g_0(z) + z - \mathcal{G}.$$

On the other hand, if $\widetilde{\mathcal{M}}_1 = 0$, then either $\widetilde{\mathcal{M}}_2 = 0$ or $z = 0$. $\widetilde{\mathcal{M}}_1 = \widetilde{\mathcal{M}}_2 = 0$ implies that $z = 0$ and $\tilde{\gamma}_3(z) = 0$. Therefore, solving (4.14) and (4.15) are equivalent when $z \in \mathbb{C} \setminus \{0\}$.

The next step is to take $z \in \mathbb{R}$ and determine whether or not there exists a real root for which $z_0 > (\gamma/2)^2$. If so, then the steady-state solution of the synaptic coupling model is unstable. Notice that $g_0(z)$ is a real-valued function on $z \in \mathbb{R}$. Hence, the points of intersection of the functions $y = g_0(z)$ and $y = -z + \mathcal{G}$ are the solutions of (4.15) on the real axis; see Figure 4.3. There exists a root $\{z, z > (\gamma/2)^2\}$ if and only if

$$(4.16) \quad -\left(\frac{\gamma}{2}\right)^2 + \mathcal{G}(\gamma) > g_0\left(\left|\frac{\gamma}{2}\right|^2\right) \iff \gamma > |\gamma| \cdot \frac{\widetilde{\mathcal{M}}_2}{\widetilde{\mathcal{M}}_1}(|\gamma/2|^2).$$

On the other hand, for $\gamma \neq 0$

$$\widetilde{\mathcal{M}}_1 = \theta \sinh(L|\gamma|/2) + \frac{|\gamma|}{2} [\cosh(L|\gamma|/2) + \operatorname{sgn}(\gamma) \sinh(L|\gamma|/2)] > 0$$

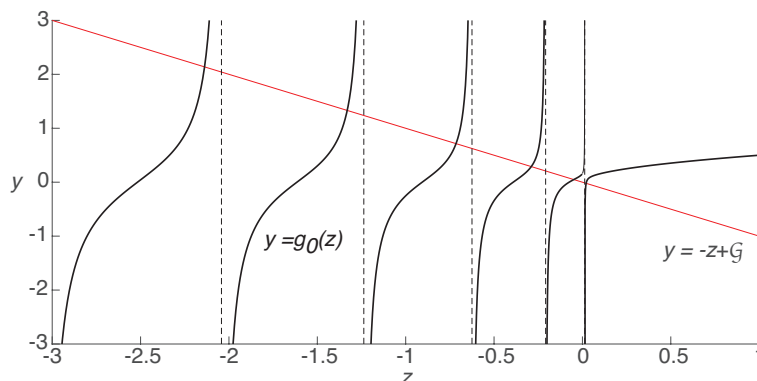


FIG. 4.3. Intersection of $y = g_0(z)$ and $y = -z + \mathcal{G}(\gamma)$ on $z \in \mathbb{R}$ for synaptic coupling model. The black solid line depicts the graph of $y = g_0(z)$, and the dotted lines are its asymptotic lines. The red line depicts the graph of $y = -z + \mathcal{G}(\gamma)$.

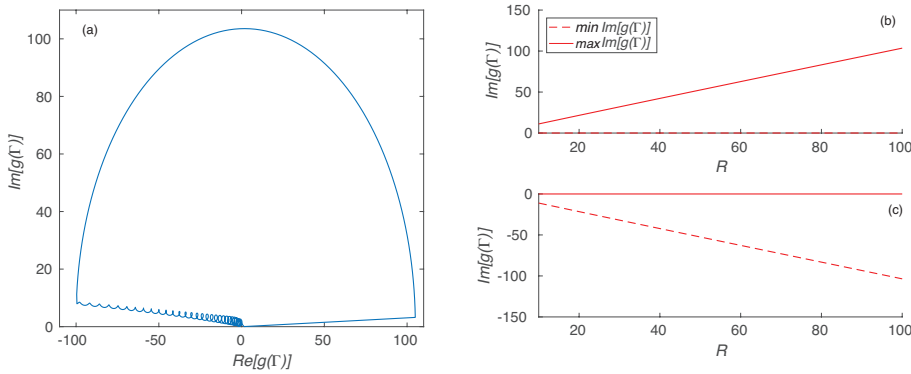


FIG. 4.4. Counting winding number of $y = g_0(z) + z - \mathcal{G}$ with contour described in Figure 4.2(a). (a) Image of the contour with $R = 100$ and $\delta = \pi/100$. (b) Maximum and minimum of the imaginary part of the image of contour in the upper-half complex plane as a function of R . The image of contour is on the upper-half plane. (c) Maximum and minimum of the imaginary part of the image of the contour reflected into the lower-half complex plane as a function of R . The image of the contour is also in the lower-half plane.

with positive constant $\theta = \gamma_3(0) - \gamma/2$ and $\text{sgn}(\gamma) = \gamma/|\gamma|$, that is,

$$|\gamma| \frac{\widetilde{\mathcal{M}}_2}{\widetilde{\mathcal{M}}_1} (|\gamma/2|^2) - \gamma = \frac{|\gamma| \cdot \theta \cdot [\cosh(L|\gamma|/2) - \text{sgn}(\gamma) \sinh(L|\gamma|/2)]}{\widetilde{\mathcal{M}}_1 (|\gamma/2|^2)} > 0.$$

That is,

$$\gamma < |\gamma| \cdot \frac{\widetilde{\mathcal{M}}_2}{\widetilde{\mathcal{M}}_1} (|\gamma/2|^2)$$

for all $\gamma \neq 0$. This contradicts (4.16), which implies that all real roots satisfy the required stability condition.

We now consider the remaining case $\{z, \text{Im}(z) \neq 0\}$. Again it can be shown that there exist no complex-valued roots using a winding number argument. However, this now has to be implemented numerically. The image of the contour depicted in Figure 4.2(a) is plotted in Figure 4.4 for $g(z) = g_0(z) + z - \mathcal{G}$, which clearly does not wind around the origin.

4.3. Accumulation time and eigenvalues. Given the eigenpairs (λ_i, ψ_i) , we can decompose the solution $C_1(t)$ as

$$(4.17) \quad C_1(t) = C_1^* + \sum_{i=1}^{\infty} e^{\lambda_i t} E_i \psi_i,$$

where E_i are coefficients and we have ordered the eigenvalues such that $0 > \lambda_1 > \lambda_2 \geq \lambda_3 \dots$. The initial condition $C_1(0) = 0$ implies that $\sum_{i=1}^{\infty} E_i \psi_i = -C_1^*$. It follows that at large times the dominant eigenmode is ψ_1 and the corresponding decay time is $\tau_{\lambda_1} = 1/|\lambda_1|$. The latter can be obtained numerically by solving either (4.7) or (4.14) on the real line. In Figure 4.5 we plot the decay time τ_{λ_1} as a function of L for both direct and synaptic coupling, and we compare our results with the accumulation time τ_1 calculated in section 3. It can be seen that the decay time is less than the accumulation time. This can be explained by noting that the eigenvalue expansion of the accumulation time τ_1 is given by $\tau_1 = \sum_{i=1}^{\infty} \tau_{\lambda_i} \psi_i$, where $\tau_{\lambda_i} = 1/|\lambda_i|$

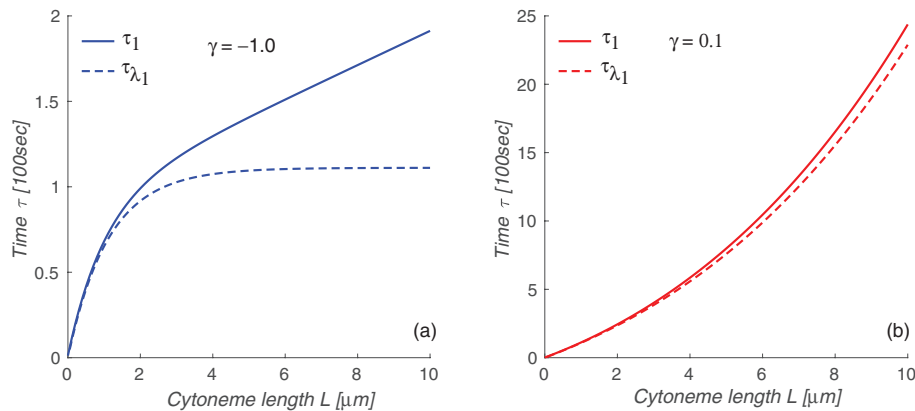


FIG. 4.5. Accumulation time τ_1 and decay time τ_{λ_1} of direct coupling model for a single target cell. The solid line depicts the accumulation time, and the dotted line represents the decay time as a function of L . (a) If $\gamma < 0$ so that $v > 0$, then the decay time converges to a finite value. (b) If $\gamma > 0$ so that $v < 0$, then the decay time increases and tends to infinity as $L \rightarrow \infty$. Other parameter values are the same as in Figure 2.3.

and $\tilde{\psi}_i = E_i \psi_i / \sum_j E_j \psi_j = -E_i \psi_i / C_1^*$. Hence, the accumulation time is a convex combination of the decay times τ_{λ_i} .

The discrepancy between the accumulation time and decay time is particularly significant when $v > 0$ ($\gamma < 0$). This is a consequence of the fact that $\lim_{L \rightarrow \infty} \tau_1 = \infty$, whereas $\lim_{L \rightarrow \infty} \tau_{\lambda_1} < \infty$. For example, consider (4.7) for the direct coupling case. The principle eigenvalue is given by the point of intersection on the positive branch of the function $y = f_0(z)$. If $z > 0$, then $\lim_{L \rightarrow \infty} f_\tau(z) = \kappa\sqrt{z}$. Thus, for large L , the positive root is approximately given by the solution to

$$(4.18) \quad \kappa\sqrt{z} = -z + \mathcal{G}$$

and depends on the sign of γ and \mathcal{G} . It follows that

$$(4.19) \quad \lim_{L \rightarrow \infty} \tau_{\lambda_1}(L) = \begin{cases} \infty, & \gamma > 0, \\ 1/\kappa(v - \kappa D), & 0 > \gamma \geq -2\kappa, \\ 4D/v^2, & -2\kappa > \gamma; \end{cases}$$

see Figure 4.5. Finally, in the case of synaptic coupling, (4.14) has the same limiting behavior as (4.7), so that

$$\lim_{L \rightarrow \infty} \tau_{\lambda_1, syn}(L) = \lim_{L \rightarrow \infty} \tau_{\lambda_1}(L).$$

5. Stochastically gated direct coupling and switching boundary conditions. Let us return to the original direct coupling model, but now assume that the transfer of vesicles from the cytoneme tip to the target cell is stochastically gated. This is motivated by the observation that many cytonemes are not static objects, but dynamically grow and shrink, resulting in more temporary contacts with target cells. (This isn't necessarily inconsistent with our static model because all we require is that there is cytoneme-mediated contact between the source and target cells for a sufficient time, comparable to the accumulation time. Moreover, there is evidence that cytonemes can be stabilized by their targets [5]. Nevertheless, it is important to

understand the possible effects of dynamic tips, particularly as details of cytoneme contacts are still not well known.)

We incorporate a stochastic gate into our transport model by taking the right-hand boundary condition to be of the form

$$(5.1) \quad u(L, t) = -(1 - m(t)) \frac{1}{\gamma} \frac{\partial u(L, t)}{\partial x},$$

where $m(t) \in \{0, 1\}$ evolves according to the two-state Markov process $0 \xrightleftharpoons[\alpha]{\beta} 1$ with transition rates α, β . The corresponding stationary probabilities of the two states are

$$(5.2) \quad \rho_0 = \frac{\alpha}{\alpha + \beta}, \quad \rho_1 = \frac{\beta}{\alpha + \beta},$$

respectively. If $m(t) = 0$, then the gate is closed and the right-hand boundary is reflecting. On the other hand, if $m(t) = 1$, then the gate is open and the right-hand boundary is absorbing as in section 2. The stochastic boundary condition together with (2.1) yields a stochastic hybrid system, more specifically a piecewise deterministic PDE.

5.1. First-order moment equations. We would like to determine the effect of switching on the mean flux through the cytoneme. This requires solving the first-order moment equations of our piecewise deterministic PDE, which can be obtained using the “method of lines” developed by Bressloff and Lawley [6, 7]. The latter involves spatially discretizing the PDE and constructing the differential Chapman–Kolmogorov equation for the resulting finite-dimensional stochastic hybrid system. This can then be used to derive the desired moment equations, after retaking the continuum limit. One additional feature of the cytoneme transport model is that the left-hand boundary condition in (2.2) couples the PDE to the compartmental variable $C_0(t)$, which evolves according to (2.3). Hence, it is necessary to introduce first-order moments of this additional piecewise deterministic variable.

In light of the above, define the first-order moments of the density $u(x, t)$ by

$$(5.3) \quad V_m(x, t) = \mathbb{E} [u(x, t) 1_{m(t)=m}], \quad m = 0, 1.$$

where $1_{m(t)=m} = 1$ if $m(t) = m$ and is zero otherwise. Expectation is taken with respect to different realizations of the stochastic gate over the interval $[0, t)$. In the same fashion, one can define the first-order moments of the vesicle concentration in the source cell according to

$$(5.4) \quad R_m(x, t) = \mathbb{E} [C_0(t) 1_{m(t)=m}], \quad m = 0, 1.$$

Following along similar lines to [6], one obtains the following coupled system of first-order moment equations:

$$(5.5a) \quad \frac{\partial V_0}{\partial t} = -\frac{\partial}{\partial x} \left(vV_0 - D \frac{\partial V_0}{\partial x} \right) + \alpha V_1 - \beta V_0,$$

$$(5.5b) \quad \frac{\partial V_1}{\partial t} = -\frac{\partial}{\partial x} \left(vV_1 - D \frac{\partial V_1}{\partial x} \right) - \alpha V_1 + \beta V_0$$

and

$$(5.6a) \quad \frac{dR_0}{dt} = \rho_0 Q - \mathcal{J}_0(0, t) + \alpha R_1 - \beta R_0,$$

$$(5.6b) \quad \frac{dR_1}{dt} = \rho_1 Q - \mathcal{J}_1(0, t) - \alpha R_1 + \beta R_0,$$

where the first-order moments of the flux along the cytoneme are

$$(5.7) \quad \mathcal{J}_m(x, t) := \mathbb{E} [J(x, t) 1_{m(t)=m}] = vV_m(x, t) - D \frac{\partial V_m}{\partial x}.$$

The corresponding boundary conditions are

$$(5.8a) \quad V_m(0, t) = \kappa R_m(t),$$

$$(5.8b) \quad V_m(L, t) = -(1 - m) \frac{1}{\gamma} \frac{\partial V_m(L, t)}{\partial x}.$$

Once these moment equations have been solved, one can determine the unconditional first-order moments $V(x, t) = V_0(x, t) + V_1(x, t)$, $\mathcal{J}(x, t) = \mathcal{J}_0(x, t) + \mathcal{J}_1(x, t)$, and $R(t) = R_0(t) + R_1(t)$.

5.2. Stationary solution. We now calculate the effective conductance $w_{\text{eff}}(L)$ defined according to the ratio

$$(5.9) \quad w_{\text{eff}} = \frac{Q}{R^*}$$

with R^* the stationary solution of the mean morphogen concentration in the source cell. First, adding (5.5a) and (5.5b) and taking time derivative to zero yields

$$0 = -\frac{\partial}{\partial x} \left(vV - D \frac{\partial V}{\partial x} \right),$$

which implies

$$(5.10) \quad vV(x) - D \frac{\partial V(x)}{\partial x} = \mathcal{J}^*$$

with \mathcal{J}^* a constant. Adding the stationary versions of (5.6a) and (5.6b) implies that $\mathcal{J}(0) = Q$ and, hence, $\mathcal{J}^* = Q$. The corresponding left-hand boundary condition in the steady-state is $V(0) = \kappa R^*$ so that

$$(5.11) \quad V(x) = \kappa R^* e^{-\gamma x} + \frac{Q}{v} (1 - e^{-\gamma x}).$$

The complexity of the switching boundary conditions is reflected by the fact that the right-hand boundary condition for V is $V(L) = V_0(L)$, that is, we now have to solve the steady-state version of (5.5a) for $V_0(x)$ —this will then allow us to obtain an explicit expression for R^* by setting $x = L$ in (5.11). After setting $V_1 = V - V_0$ and rearranging, we have

$$(5.12) \quad D \frac{\partial^2 V_0}{\partial x^2} - v \frac{\partial V_0}{\partial x} - (\alpha + \beta) V_0 = \alpha V(x).$$

This has the general solution

$$(5.13) \quad V_0(x) = R^* e^{-\gamma x} (A e^{\gamma_1 x} + B e^{\gamma_2 x}) + \rho_0 V(x),$$

where A, B are constants to be determined and

$$\gamma_i = \frac{1}{2} \left[\gamma \pm \sqrt{\gamma^2 + 4(\alpha + \beta)/D} \right], \quad i = 1, 2.$$

This is supplemented by the boundary conditions $V_0(0) = \kappa R_0^*$ and $\mathcal{J}_0(0) = 0$. Setting $R_0^* = \eta R^*$ for some η , we then have three unknown constants A, B, η . Hence, we need to obtain three independent equations for these coefficients.

First, setting $x = 0$ in (5.13) and imposing the left-hand boundary condition $V_0(0) = \kappa\eta R^*$ and dividing through by R^* gives

$$(5.14) \quad A + B - \kappa\eta = -\kappa\rho_0.$$

Second, substituting the general solution (5.13) into the right-hand boundary condition for $V_0(L)$ (see (5.8b)), implies that

$$0 = -DR^*e^{-\gamma L} (A\gamma_1e^{\gamma_1L} + B\gamma_2e^{\gamma_2L}) + \rho_0Q,$$

which, after rearranging, yields

$$(5.15) \quad \gamma_1e^{\gamma_1L}A + \gamma_2e^{\gamma_2L}B = \frac{\rho_0e^{\gamma L}Q}{DR^*}.$$

Third, substituting the general solution (5.13) into the stationary version of (5.6a) and setting $x = 0$ yields

$$0 = \rho_0Q - [-R^*D(A\gamma_1 + B\gamma_2) + \rho_0Q] + \alpha(1 - \eta)R^* - \beta\eta R^*,$$

which reduces to the equation

$$\gamma_1A + \gamma_2B - \frac{\alpha + \beta}{D}\eta = -\frac{\alpha}{D}.$$

Finally, using the fact that $\gamma_1\gamma_2 = -(\alpha + \beta)/D$ leads to

$$(5.16) \quad \gamma_1A + \gamma_2B + \gamma_1\gamma_2\eta = \rho_0\gamma_1\gamma_2.$$

The three equations (5.14), (5.15), and (5.16) form a system of linear equations with three unknowns A, B , and η . Using (5.14) to eliminate B in (5.15) and (5.16) gives

$$(5.17a) \quad [\gamma_1e^{\gamma_1L} - \gamma_2e^{\gamma_2L}]A + \gamma_2e^{\gamma_2L}\kappa\eta = \frac{\rho_0e^{\gamma L}Q}{DR^*} + \gamma_2e^{\gamma_2L}\kappa\rho_0,$$

$$(5.17b) \quad A\Delta\gamma + (\kappa + \gamma_1)\gamma_2\eta = (\kappa + \gamma_1)\gamma_2\rho_0,$$

where $\Delta\gamma = \gamma_1 - \gamma_2$. Solving (5.17a) and (5.17b) for η gives

$$(5.18) \quad \eta = \frac{\rho_0}{\Gamma(L)} \left[\Gamma(L) - \frac{\Delta\gamma e^{\gamma L}Q}{DR^*} \right],$$

where

$$\Gamma(L) := [\mathcal{A}_1(L)(\kappa + \gamma_1)\gamma_2 - \Delta\gamma \cdot \gamma_2e^{\gamma_2L}\kappa] = \gamma_1\gamma_2(\kappa\mathcal{A}_0(L) + \mathcal{A}_1(L)),$$

and we have introduced the functions

$$(5.19) \quad \mathcal{A}_0(L) = e^{\gamma_1L} - e^{\gamma_2L}, \quad \mathcal{A}_1(L) = \gamma_1e^{\gamma_1L} - \gamma_2e^{\gamma_2L}.$$

Having determined η we can then determine the coefficients A, B .

In order to complete the analysis we still need to calculate $V_0(L)$. For convenience, we take $V_0(L) = \kappa R^* \xi$. Setting $x = L$ in (5.13) then yields

$$\kappa R^* \xi = R^* e^{-\gamma L} (A e^{\gamma_1 L} + B e^{\gamma_2 L}) + \rho_0 \kappa R^* \xi,$$

which reduces to the equation

$$\mathcal{A}_0(L)A = \kappa \rho_1 e^{\gamma L} \xi + e^{\gamma_2 L} \kappa (\rho_0 - \eta).$$

Substituting for A using (5.17b) gives

$$\frac{(\kappa + \gamma_1)\gamma_2(\rho_0 - \eta)}{\gamma_1 - \gamma_2} \mathcal{A}_0(L) = \kappa \rho_1 e^{\gamma L} \xi + e^{\gamma_2 L} \kappa (\rho_0 - \eta),$$

which can be rearranged to yield

$$(5.20) \quad \gamma_1 \gamma_2 (\kappa \mathcal{A}_2(L) + \mathcal{A}_0(L)) (\rho_0 - \eta) = \Delta \gamma \cdot \kappa \rho_1 e^{\gamma L} \xi,$$

where

$$(5.21) \quad \mathcal{A}_2(L) = \frac{e^{\gamma_1 L}}{\gamma_1} - \frac{e^{\gamma_2 L}}{\gamma_2}.$$

We now substitute for η in (5.20) using (5.18) to obtain the result

$$(5.22) \quad \kappa v R^* \xi = -\frac{\gamma \rho_0 \mathcal{B}_1 Q}{\rho_1 \mathcal{B}_0}.$$

Finally, setting $x = L$ in (5.11),

$$(5.23) \quad \kappa R^* \xi v = \kappa v e^{-\gamma L} R^* + Q (1 - e^{-\gamma L}),$$

and combining with (5.22), we find that $R^* = Q/w_{\text{eff}}(L)$ with

$$(5.24) \quad w_{\text{eff}}(L) = \frac{\kappa v e^{-\gamma L} \cdot \rho_1 \mathcal{B}_0(L)}{(e^{-\gamma L} - 1) \rho_1 \mathcal{B}_0(L) - \gamma \rho_0 \mathcal{B}_1(L)}.$$

Example plots comparing the effective conductance with switching and the conductance without switching are shown in Figure 5.1(a).

Two additional results follows from the above analysis. First, the asymptotic ratio $\lim_{L \rightarrow \infty} w_{\text{eff}}(L)/w(L)$ depends on the sign of v ; see Figure 5.1(b). If $v > 0$, then $w_{\text{eff}}(L)/w(L)$ converges to one as cytoneme length tends to infinity. That is, the switching boundary condition for a sufficiently long cytoneme gives the same conductance as a fixed absorbing boundary condition. This reflects the fact that for positive speeds v , the dynamics at the tip is dominated by advection. On the other hand, if $v < 0$, then we have

$$(5.25) \quad \lim_{L \rightarrow \infty} \frac{w_{\text{eff}}(L)}{w(L)} = \rho_1 \cdot \frac{1}{\rho_1 + \rho_0 \gamma / \gamma_1},$$

where

$$\frac{\gamma}{\gamma_1} = \frac{2}{1 + \sqrt{1 + 4(\alpha + \beta)D/|v|^2}}.$$

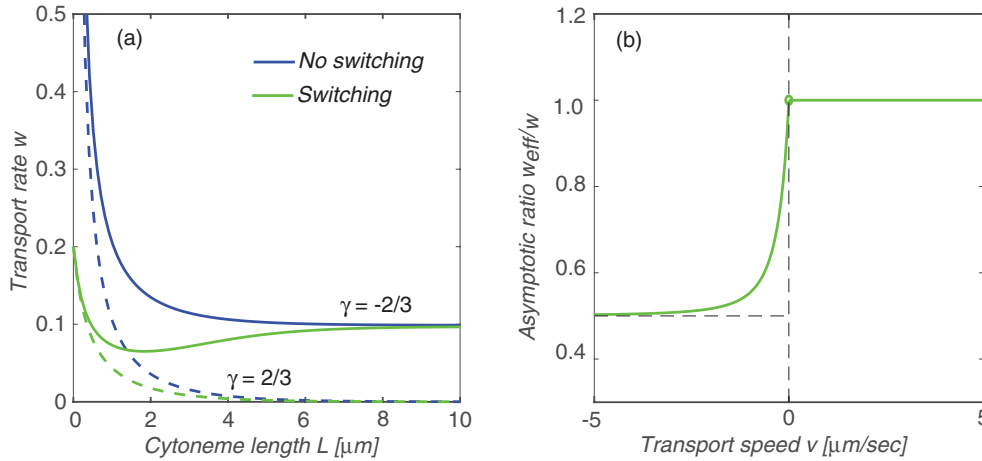


FIG. 5.1. (a) Transport rates $w_0(L)$, $w_1(L)$, and $w_s(L)$ plotted as a function of cytoneme length L for $\gamma > 0$ and $\gamma < 0$. (b) Asymptotic ratio of transport rate $w_{\text{eff}}(L)$ to $w(L)$ plotted as a function of average transport velocity v . If $v < 0$, then the ratio converges to ρ_1 as $|v|$ tends to infinity. On the other hand, if $v > 0$, then the ratio is always one. Same parameter values as in Figure 2.3.

If $(\alpha + \beta)D \ll |v|$, then $\gamma/\gamma_1 \approx 1$. It follows that the asymptote converges to ρ_1 , the stationary probability of the absorbing boundary state. This reflects the fact that for negative speeds, the dynamics at the tip is dominated by diffusion. The second observation is that w_{eff} converges to w in the fast switching limit. For fixed L , taking $\alpha, \beta \rightarrow \infty$ gives

$$(5.26) \quad \lim_{\alpha, \beta \rightarrow \infty} \frac{w_{\text{eff}}(L)}{w(L)} = \frac{e^{-\gamma L} - 1}{e^{-\gamma L} - 1 - \gamma \lim_{\alpha, \beta \rightarrow \infty} \alpha \mathcal{B}_1(\alpha, \beta) / \beta \mathcal{B}_0(\alpha, \beta)}$$

with

$$\lim_{\alpha, \beta \rightarrow \infty} \frac{\alpha \mathcal{B}_1(\alpha, \beta)}{\beta \mathcal{B}_0(\alpha, \beta)} = 0.$$

This establishes that the ratio converges to one in the fast switching limit. That is, the switching transport rate converges to the open-gated transport rate for fixed L in the fast switching limit. This is consistent with previous examples of diffusion in switching environments [6].

6. Discussion. In this paper, we analyzed a one-dimensional advection-diffusion model of morphogen transport along cytonemes, comparing the effects of direct vs. synaptic contacts between cytoneme tips and target cells. One important parameter in our analysis was $\gamma = -v/D$, where v is the advection speed and D the effective diffusivity of morphogen carrying vesicles within the cytoneme. Both the sign and magnitude of γ had a strong affect on the asymptotic behavior of the steady-state morphogen concentration, as well as the approach to steady-state. One major conclusion of our analysis is that synaptic contacts allow for longer-range interactions than direct contacts. Although most of our analysis assumed that the contact between the cytoneme tip and a target cell was static, we considered a dynamic tip in section 5, which we modeled in terms of a randomly switching boundary condition, and we showed that this could lead to a nonmonotonically varying concentration profile. The dynamic nature of cytonemes raises another interesting issue that we hope to explore

in future work, namely, the process whereby cytonemes find their target cells in the first place. It has been suggested that this could occur either via a random search process based on retraction and growth or via some chemoattractant [13]. There are certain similarities with microtubules of the mitotic spindle searching for kinetochores prior to separation of cytochrome pairs via catastrophes [28], although one major difference is that cytonemes are actin-based.

REFERENCES

- [1] H. L. ASHE AND J. BRISCOE, *The interpretation of morphogen gradients*, Development, 133 (2006), pp. 385–394.
- [2] A. M. BEREZHKOVSII, C. SAMPLE, AND S. Y. SHVARTSMAN, *How long does it take to establish a morphogen gradient?*, Biophys. J., 99 (2010), pp. L59–L61.
- [3] A. M. BEREZHKOVSII, C. SAMPLE, AND S. Y. SHVARTSMAN, *Formation of morphogen gradients: Local accumulation time*, Phys. Rev. E, 83 (2011), 051906.
- [4] M. BISCHOFF, A. C. GRADILLA, I. SEIJO, G. ANDRES, C. RODRIGUEZ-NAVAS, L. GONZALEZ-MENDEZ, AND I. GUERRERO *Cytonemes are required for the establishment of a normal Hedgehog morphogen gradient in Drosophila epithelia*, Nat. Cell Biol., 15 (2013), pp. 1269–1281.
- [5] W. J. BODEEN, S. MARADA, A. TRUONG, AND S. K. OGDEN, *A fixation method to preserve cultured cell cytonemes facilitates mechanistic interrogation of morphogen transport*, Development, 144 (2017), pp. 3612–3624.
- [6] P. C. BRESSLOFF AND S. D. LAWLEY, *Moment equations for a piecewise deterministic PDE*, J. Phys. A, 48 (2015), 105001.
- [7] P. C. BRESSLOFF AND S. D. LAWLEY, *Escape from subcellular domains with randomly switching boundaries*, Multiscale Model. Simul., 13 (2015), pp. 1420–1455.
- [8] P. C. BRESSLOFF, *Diffusion in cells with stochastically gated gap junctions*, SIAM J. Appl. Math., 76 (2016), pp. 1658–1682.
- [9] P. C. BRESSLOFF AND H. KIM, *Bidirectional transport model of morphogen gradient formation via cytonemes*, Phys. Biol., 15 (2018), 026010.
- [10] M. BUSZCZAK, M. INABA, AND Y. M. YAMASHITA, *Signaling by cellular protrusions: Keeping the conversation private*, Trends Cell Biol., 26 (2016), pp. 526–534.
- [11] C. L. FAIRCHILD AND M. BARNA, *Specialized filopodia: At the tip of morphogen transport and vertebrate tissue patterning*, Current Opin. Genet. Dev., 27 (2014), pp. 67–73.
- [12] A. C. GRADILLA AND I. GUERRERO, *Cytoneme-mediated cell-to-cell signaling during development*, Cell Tissue Res., 352 (2013), pp. 59–66.
- [13] T. B. KORNBERG, *Cytonemes and the dispersion of morphogens*, Wiley Interdiscip. Rev. Dev. Biol., 3 (2014), pp. 445–463.
- [14] T. B. KORNBERG AND S. ROY, *Cytonemes as specialized signaling filopodia*, Development, 141 (2014), pp. 729–736.
- [15] A. D. LANDER, W. C. LO, AND F. Y. WAN, *Do morphogen gradients arise by diffusion?*, Dev. Cell., 2 (2002), pp. 785–796.
- [16] A. D. LANDER, *Pattern, growth and control*, Cell, 144 (2011), pp. 955–969.
- [17] J. M. NEWBY AND P. C. BRESSLOFF, *Quasi-steady state reduction of molecular-based models of directed intermittent search*, Bull. Math. Biol., 72 (2010), pp. 1840–1866.
- [18] F. A. RAMIREZ-WEBER AND T. B. KORNBERG, *Cytonemes: Cellular processes that project to the principal signaling center in Drosophila imaginal discs*, Cell, 97 (2009), pp. 599–607.
- [19] S. ROY, F. HSIUNG, AND T. B. KORNBERG, *Specificity of Drosophila cytonemes for distinct signaling pathways*, Science, 332 (2011), pp. 354–358.
- [20] T. A. SANDERS, E. LLAGOSTERA, AND M. BARNA, *Specialized filopodia direct long-range transport of SHH during vertebrate tissue patterning*, Nature, 497 (2013), pp. 628–632.
- [21] F. P. SAGAR AND M. SCAAL, *Signaling filopodia in vertebrate embryonic development*, Cell Mol. Life Sci., 73 (2016), pp. 961–974.
- [22] S. Y. SHVARTSMAN AND R. E. BAKER, *Mathematical models of morphogen gradients and their effects on gene expression*, Wiley Interdiscip. Rev. Dev. Biol., 1 (2012) pp. 715–730.
- [23] E. STANGANELLO, A. I. HAGEMANN, B. MATTES, C. SINNER, D. MEYEN, S. WEBER, A. SCHUG, E. RAZ, AND S. SCHOLPP, *Filopodia-based Wnt transport during vertebrate tissue patterning*, Nat. Commun., 6 (2015), 5846.
- [24] E. STANGANELLO AND S. SCHOLPP, *Role of cytonemes in WNT transport*, J. Cell Sci., 129 (2016), pp. 665–672.

- [25] H. TEIMOURI AND A. B. KOLOMEISKY, *New model for understanding mechanisms of biological signaling: Direct transport via cytonemes*, J. Phys. Chem. Lett., 7 (2016), pp. 180–185.
- [26] H. TEIMOURI AND A. B. KOLOMEISKY, *Mechanisms of the formation of biological signaling profiles*, J. Phys. A, 49 (2016), 483001.
- [27] O. WARTLICK, A. KICHEVA, AND M. GONZALEZ-GAITAN, *Morphogen gradient formation*, Cold Spring Harbor Perspect. Biol., 1 (2009), a001255.
- [28] R. WOLLMAN, E. N. CYTYNBAUM, J. T. JONES, T. MEYER, J. M. SCHOLEY, AND A. MOGILNER, *Efficient chromosome capture requires a bias in the ‘search-and-capture’ process during mitotic-spindle assembly*, Curr. Biol., 15 (2005), pp. 828–832.
- [29] L. WOLPERT, *Positional information and the spatial pattern of cellular differentiation*, J. Theor. Biol., 25 (1969), pp. 1–47.